



# Comparison of three real time techniques for the measurement of dynamic fracture initiation toughness in metals

D.D. Anderson <sup>a,\*</sup>, A.J. Rosakis <sup>b</sup>

<sup>a</sup> General Electric Global Research Center, One Research Circle, Niskayuna, NY 12309, USA

<sup>b</sup> Graduate Aeronautical Laboratories, California Institute of Technology, Pasadena, CA 91125, USA

Received 7 October 2003; received in revised form 15 April 2004; accepted 18 April 2004

Available online 20 July 2004

## Abstract

Three techniques for measuring dynamic stress intensity factor time histories of dynamically loaded stationary mode-I cracks are compared as applied to dynamically loaded pre-cracked 6Al–4V titanium alloy specimens. The three techniques are crack opening displacement (COD), dynamic strain gage measurement, and coherent gradient sensing (CGS). The stress intensity factor histories are inferred from each measurement technique and are used to obtain the critical dynamic initiation toughness as a function of loading rate ( $K_{Ic}^d(K_I^d)$ ). There are significant differences in implementation and information obtained from each of the three measurement techniques, though for the tests performed all are found to yield very similar results.

© 2004 Elsevier Ltd. All rights reserved.

*Keywords:* Dynamic fracture mechanics; Dynamic initiation toughness; Crack opening displacement; Coherent gradient sensing

## 1. Introduction

The origin of the stress intensity factor used to describe the magnitude of crack tip stresses dates back to 1957 due to work by Irwin [1] and Williams [2] with asymptotic linear elastic crack tip solutions. With this parameter, a material's fracture toughness can be established by measuring the stress intensity factor at incipient crack initiation. Standards for determining and validating a material's critical stress intensity factor for initiating a quasistatically loaded stationary crack (ASTM E399 [3]) have made fracture toughness determination routine for structural materials. However, as with other mechanical properties, fracture toughness may be rate dependent. Thus safe and effective use of materials where dynamic loading may occur and fracture is of concern requires that the relationship between some appropriate measure of loading rate and fracture toughness is understood. In some materials such as aluminum, fracture toughness

\* Corresponding author. Tel./fax: +1-518-387-7292.

E-mail addresses: [anderson@research.ge.com](mailto:anderson@research.ge.com) (D.D. Anderson), [rosakis@aero.caltech.edu](mailto:rosakis@aero.caltech.edu) (A.J. Rosakis).

at some dynamic loading rates may be *less* than its quasistatic fracture toughness, thus designing to quasistatic values may be non-conservative and unsafe.

Previous work on measuring material dynamic fracture properties is very limited. Most dynamic failure studies have utilized materials with properties ideal for experimentation, typically polymers. For example, dynamically loaded Homalite-100 fracture properties were studied using the optical method of caustics by Ravi-Chandar and Knauss [4]. Dynamic crack initiation in PMMA was studied by Rittel and Maigre [5–7] using a novel hybrid analytical/experimental procedure. Transient crack growth in PMMA was examined using CGS by Freund and Rosakis [8]. Dynamic crack growth research of polymers using dynamic photoelasticity is described by Dally [11]. Ceramic material was tested by Suresh et al. [9]. Prior work on engineering materials is limited to simple observations. For example, critical crack opening displacements for explosively loaded 1020 hot-rolled steel were obtained by Wilson et al. [10]. Two of the first studies of dynamic crack growth on metals were conducted by Rosakis et al. [12] and Zehnder and Rosakis [13] who examined highly dynamic crack growth in thick plates of AISI 4340 steel using the optical method of caustics in reflection in conjunction with high speed photography. Recently, dynamic initiation and propagation behavior in thin aluminum sheets was studied by Owen et al. [14]. Small specimens were loaded using a split Hopkinson bar and the stress intensity factor  $K_I^d$  was calculated using boundary measurements by assuming quasiequilibrium. This assumption was validated by real time dynamic COD measurements from the thinnest sheets. An invaluable reference on all things related to dynamic fracture mechanics is by Freund [29].

This work describes the first time that multiple techniques are simultaneously used to measure dynamic crack initiation toughnesses of an engineering material with ductility. Dynamic fracture experiments using crack opening displacement (COD), strain gage measurement, and coherent gradient sensing (CGS) measurement techniques were conducted on drop weight loaded commercial grade 6Al–4V titanium specimens to allow measurement cross-checking and ultimately to validate each technique's suitability. While each technique has its advantages and disadvantages, all produced remarkably comparable measurements of the material's critical stress intensity factor for crack initiation,  $K_{Ic}^d$ .

## 2. Basis for a fracture toughness parameter

Linear elastic fracture mechanics (LEFM) serves as a simple but sufficient analytical framework for studying fracture behavior engineering materials so long as ductility is not too great. For each LEFM crack mode, stress fields satisfying the boundary condition of having traction-free crack faces are asymptotic with unknown coefficients reflecting unspecified far-field boundary conditions [1,26–28] are of the form:

$$\sigma_{ij} = \left( \frac{K}{\sqrt{2\pi r}} \right) f_{ij}(\theta) + \sum_{m=0}^{\infty} A_m r^{m/2} g_{ij}^{(m)}(\theta) \quad (1)$$

where  $\sigma_{ij}$  are Cartesian components of the stress tensor,  $r$  and  $\theta$  are spatial coordinates with respect to the usual crack tip coordinate system (Fig. 1),  $f_{ij}$  and  $g_{ij}^{(m)}$  are functions of  $\theta$ , and  $K$  and  $A_m$  are the coefficients of the singular and higher order terms respectively.  $f_{ij}$  and  $g_{ij}$  are known universal functions of angle  $\theta$  for all cracks propagating at speeds much slower than the material's shear wave speed, including stationary cracks.

For each mode the leading asymptotic term is singular and thus dominates near the crack tip. Because of this dominance, the leading term's coefficient (or magnitude) can serve as a single parameter description of the stress state at the crack tip. The coefficient  $K$  for the leading singular term is called the stress intensity factor, which is usually subscripted to specify mode, i.e.,  $K_I$ ,  $K_{II}$  or  $K_{III}$ . For dynamically loaded stationary cracks a superscript “*d*” will be used to denote the time dependence of the stress intensity factor. Its critical value at initiation of crack growth will be denoted by  $K_{Ic}^d$  (for mode I) and will be called the dynamic fracture toughness.

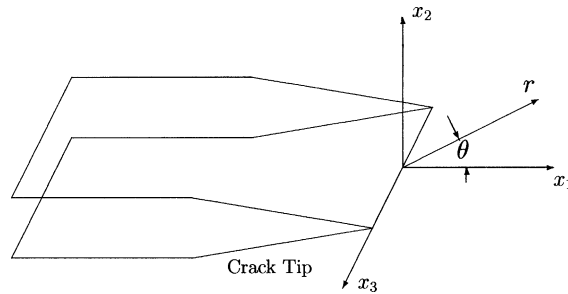


Fig. 1. Crack tip coordinate system.

A stress singularity at the crack tip as predicted by LEFM cannot realistically exist in materials with finite strength. Instead the highly stressed material yields and plastically deforms. To first order the time dependent size of the plastic zone for mode I is:

$$r_p = \frac{1}{2\pi} \left( \frac{K_I^d}{\sigma_{YS}} \right)^2 \quad (2)$$

where  $\sigma_{YS}$  is the material yield stress. At crack initiation the critical characteristic plastic zone size,  $r_{pc}$  is determined by setting  $K_I^d = K_{Ic}^d$ . The actual shape of the plastic zone depends on crack tip triaxiality. Because  $\sigma_{YS}$  is strain-rate dependent,  $r_{pc}$  is also dependent on crack tip loading rate and propagation speed, with the later effect dominant for growing cracks. If  $K_{Ic}^d$  is also found to be rate dependant, this will also influence the critical value ( $r_{pc}$ ) of  $r_p$  at initiation of crack growth by providing additional rate dependence to this critical length scale. Eq. (2) defines a useful material/rate-dependent length scale for crack tip mechanics.

In scenarios in which a crack tip stress field is well modeled by LEFM, the plastic zone is always small enough to be completely surrounded by an annulus in which stresses are described by the  $K$ -field (leading term in the asymptotic expansion). The outer extent of the  $K$ -field dominated annulus is due to the increasing relative contributions of higher order asymptotic stress field terms. However since a  $K$ -dominated annulus completely bounds the crack tip,  $K$  is still a single parameter description of the crack tip stress state because it describes the entire boundary conditions of the crack tip. This concept that LEFM can still describe crack tip fields in such cases despite crack tip yielding is called small scale yielding (S.S.Y.) [8,29]. Ignoring material yielding effects, the extend of  $K$ -field dominance is linear with the dominant structure size. Thus the applicability of S.S.Y. depends on material *and* on geometry.

Regarding the establishment of material fracture properties, for a given loading rate the initiation toughness asymptotically decreases as specimen thickness increases. The asymptotic limit is called the plane strain fracture toughness and is useful because it is conservative and geometry independent, though it is still rate dependent. Because the characteristic plastic zone size  $r_{pc}$  is in general rate dependent (either through  $\sigma_{YS}$  or through  $K_{Ic}^d$  or through both), a specimen may be thick enough to measure plane strain fracture toughness at a higher loading rate but not at a lower one.

### 3. Description of techniques

#### 3.1. Crack opening displacement

Crack opening displacement technique involves measuring opening displacements between the crack faces behind a single crack tip and using elastic plastic fracture mechanics (EPFM) to relate the opening displacements to the stress intensity factor.

### 3.1.1. Governing equations

The relationship between crack opening displacement and stress intensity factor used for this work is from Shih [15]. This relationship is obtained using the HRR crack tip solution [16,17] for power law hardening materials. For such materials the flow stress  $\sigma$  and strain  $\varepsilon$  under uniaxial loading are assumed to be related as follows:

$$\frac{\sigma}{\sigma_0} = \alpha \left( \frac{\varepsilon}{\varepsilon_0} \right)^n \quad (3)$$

where  $\alpha$  and  $n$  are material constants, the latter called the strain hardening exponent, and  $\sigma_0$  and  $\varepsilon_0$  are reference stress and strain respectively.

Employing the standard crack tip coordinate system (Fig. 1), the crack opening profile  $\delta(r, t, n)$  behind the crack tip is given by

$$\delta(r, t, n) = \alpha \varepsilon_0 \left\{ \frac{J(t)}{\alpha \sigma_0 \varepsilon_0 I_n} \right\}^{\frac{n}{n+1}} r^{\frac{1}{n+1}} \left[ 2\tilde{u}_2(\pi, n) \right] \quad (4)$$

where  $I_n$  and  $\tilde{u}_2$  are known and tabulated functions of the hardening exponent [15] and  $J(t)$  is the time-varying value of the  $J$ -integral. The  $x_1$  (horizontal) component of the displacement vector of material points on the crack faces is given by

$$u_1(r, t, n) = \alpha \varepsilon_0 \left\{ \frac{J(t)}{\alpha \sigma_0 \varepsilon_0 I_n} \right\}^{\frac{n}{n+1}} r^{\frac{1}{n+1}} \left[ 2\tilde{u}_1(\pi, n) \right] \quad (5)$$

By defining the location of COD measurement  $\delta$  to be between the points of intersection of the crack faces and radial lines from the crack tip at  $\pm 135^\circ$  (Fig. 2),

$$r - u_1 = \delta/2 \quad (6)$$

Eqs. (4)–(6) are satisfied by

$$\delta(t, n) = d_n(n) \frac{J(t)}{\sigma_0} \quad (7)$$

where  $d_n(n)$  is given by

$$d_n(n) = (\alpha \varepsilon_0)^{1/n} (\tilde{u}_1(n) + \tilde{u}_2(n))^{1/n} \frac{2\tilde{u}_2(n)}{I_n} \quad (8)$$

The coefficient  $d_n(n)$  was first calculated in [15] and shown here plotted versus strain hardening exponent in Fig. 3 (plane strain) and Fig. 4 (plane stress). For linear elastic materials under plane stress conditions  $J$  is related to the stress intensity factor  $K$  by

$$J = G = \frac{K_I^2}{E} \quad (9)$$

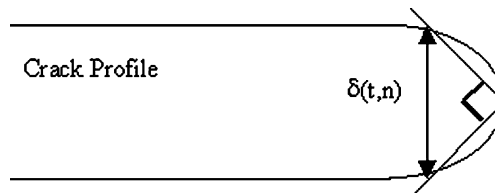


Fig. 2. Location of crack opening displacement measurement.

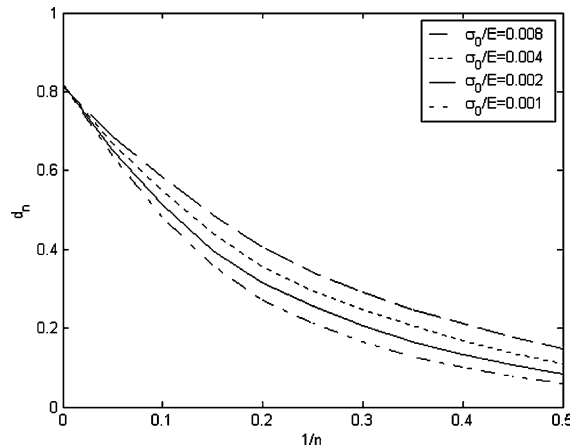


Fig. 3.  $d_n$  versus strain hardening exponent  $n$  for plane strain.

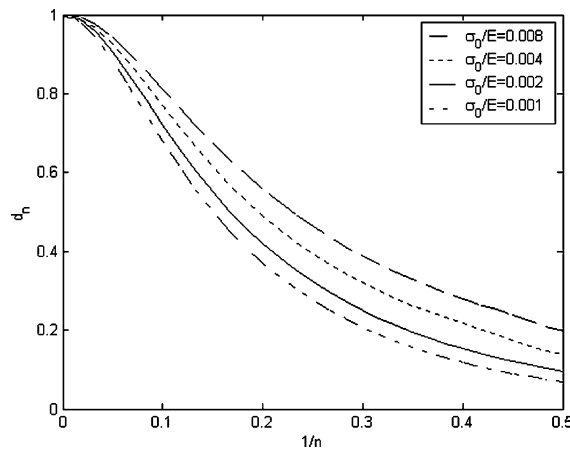


Fig. 4.  $d_n$  versus strain hardening exponent  $n$  for plane stress.

where  $G$  is the energy release rate and  $E$  is the material's modulus of elasticity. This relation requires a small scale yielding assumption through the time of crack initiation.

### 3.2. Implementation

The real time measurement of crack opening displacement generally requires some improvisation. The violent nature of the dynamic specimen impact event precludes the use of imaging optics in close proximity of the specimen. The procedure outlined in this section should be considered to be specific to this study, but it may work with adaptation with other materials. For this work the opening profile of the crack was obtained by back-lighting the specimen with an expanded collimated laser beam (Spectra-Physics Argon-Krypton-ion laser, model 166–09, operating at a wavelength of  $\lambda = 514.5$  nm) and recording the resulting profile by high speed photography (Cordin 330 rotating mirror camera, 80 images at frame rates of up to 2 million frames per second, Kodak T-Max 3200 film). Crack face roughness causes the projected profile

width to be conservative. In fact, for the specimens tested for this work, no light passed through the fatigue pre-crack area until after crack initiation. The fatigue crack extends 2 mm ahead of an EDM notch which has smooth, parallel faces which are suitable for opening displacement measurements without risk of under-measurement. The drawback is that the opening in the EDM notch must be related to the opening at the crack tip  $\delta$  as indicated in Fig. 2. For the 6Al–4V titanium tested, linear elastic perfectly plastic (LEPP) material behavior was assumed in which the crack faces open in parallel ( $n \rightarrow \infty$ , Eq. (4)). This assumption was suggested by the shape of the uniaxial stress–strain relation for this material (Fig. 5) and was directly verified by measuring the opening displacement as a function on distance behind the crack tip along the EDM notch. Fig. 6 is a typical plot of the angle between the two EDM faces as a function of elapsed time

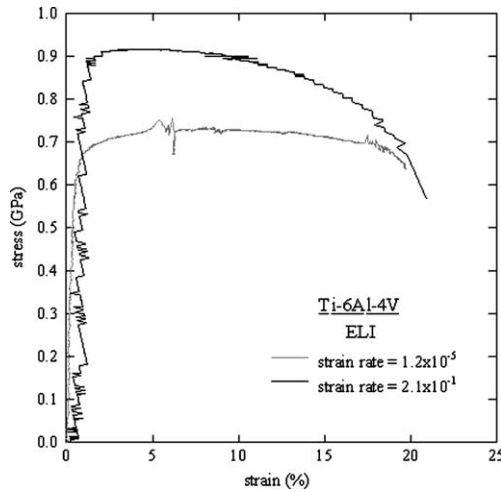


Fig. 5. Stress–strain curves for Ti 6Al–4V ELI titanium at low and high strain rates.

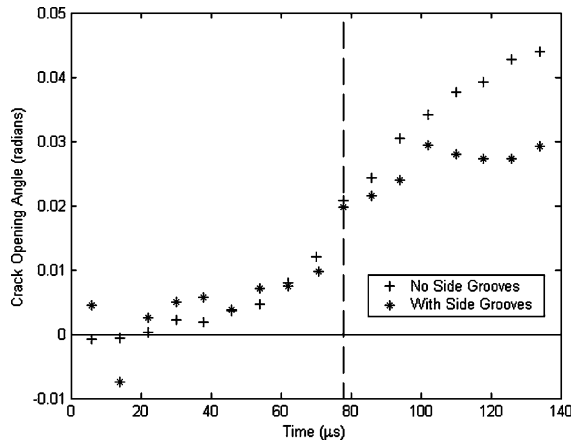


Fig. 6. Crack/EDM notch opening angle versus time for 6Al–4V Ti specimens with and without side-grooves impacted at 9 m/s. Vertical dashed line identifies the best estimate of the time of crack initiation.

after impact. The angle between the EDM faces was found to be nearly constant until initiation, at which time it jumps in value as does the rate of notch opening. This observation was used to indicate the time of crack initiation. The LEPP assumption, once demonstrated to be reasonably accurate, is also beneficial in that it greatly simplifies the relationship between notch opening and crack tip opening displacement—they are the same.

### 3.3. *Comments*

Of the three stress intensity factor measurement techniques that can be used dynamically, the real time COD method is most difficult to interpret for three reasons. First, strain hardening effects must be correctly accounted for to relate opening profile measurements in the notch to the crack tip opening displacement. This was dealt with by assuming LEPP material behavior. Second, the determination of initiation time is of paramount importance in determining fracture toughness. Typically in dynamic tests the value of the crack opening  $\delta$  increases rapidly about initiation, and small errors in the time of initiation cause large errors in the estimation of  $K_{Ic}^d$ . This initiation time was taken to coincide with a jump in notch opening and opening angle. This jump is due to the decrease in remaining ligament as the crack begins to propagate. Third, difficulties arise due to the lack of optical resolution in notch opening profile measurements. This was handled by completely automating crack profile characterization computationally using a custom made Matlab<sup>1</sup> code. These enabling assumptions and methodologies were justified both by checking for internal consistency and comparing results from identical tests using the other two measurement techniques considered in this work. Despite the difficulties and limitations of the COD technique, it has one significant advantage over the other techniques under consideration: COD measurements can be made on side-grooved specimens, making it invaluable for testing more ductile materials (still falling within SSY). Side-grooves can be utilized to obtain plane strain toughness values from specimens which would otherwise be too thin.

### 3.4. *Strain gage measurement*

The pioneering work by Dally and his coworkers (e.g. Dally and Burger [19]) has demonstrated that strain gages can be used to measure in-plane surface strain in the vicinity of cracks which can be related to analytic asymptotic stress fields to determine stress intensity factors. This method can be employed for quasistatic or dynamic loading for both initiating and propagating cracks as material behavior allows. The primary advantages of strain gages are low cost and simplicity of analysis with essentially no special specimen preparation or complex optical setup required. Strain gages can be used simultaneously with other measurement techniques for redundancy.

#### 3.4.1. *Governing equations*

In the context of the evaluation of near-crack tip strain fields, field parameters and measured strains are related as follows: for an arbitrary strain gage placement within a region of plane stress (i.e., outside the three-dimensional zone) the measured strain due to quasistatic mode I and mode II stress fields through order  $r$  is given by the following (from Dally and Burger [19]):

---

<sup>1</sup> The MathWorks, Inc., 3 Apple Hill Drive, Natick, MA 01760-2098.

$$\begin{aligned}
2\mu\varepsilon_{x'x'} = & A_0 r^{-1/2} \left[ k \cos \frac{\theta}{2} - \frac{1}{2} \sin \theta \left( \sin \frac{3\theta}{2} \cos 2\alpha - \cos \frac{3\theta}{2} \sin 2\alpha \right) \right] \\
& + B_0 (k + \cos 2\alpha) + A_1 r^{1/2} \cos \frac{\theta}{2} \left( k + \sin^2 \frac{\theta}{2} \cos 2\alpha - \frac{1}{2} \sin \theta \sin 2\alpha \right) \\
& + B_1 r [(k + \cos 2\alpha) \cos \theta - 2 \sin \theta \sin 2\alpha] + C_0 r^{-1/2} \left[ -k \sin \frac{\theta}{2} - \cos 2\alpha \left( \frac{1}{2} \sin \theta \cos \frac{3\theta}{2} + \sin \frac{\theta}{2} \right) \right. \\
& \left. - \sin 2\alpha \left( \frac{1}{2} \sin \theta \sin \frac{3\theta}{2} - \cos \frac{\theta}{2} \right) \right] + C_1 r^{1/2} \left[ k \sin \frac{\theta}{2} + \cos 2\alpha \left( \frac{1}{2} \sin \theta \cos \frac{\theta}{2} + \sin \frac{\theta}{2} \right) \right. \\
& \left. + \sin 2\alpha \left( \frac{1}{2} \sin \theta \sin \frac{\theta}{2} + \cos \frac{\theta}{2} \right) \right] + 2D_1 r [\sin \theta (k + \cos 2\alpha)] \quad (10)
\end{aligned}$$

where  $k = (1 - \nu)/(1 + \nu)$ ,  $\mu$  and  $\nu$  are the material's shear modulus and Poisson's ratio respectively,  $r$  and  $\theta$  specify the strain gage location with respect to the crack tip coordinates,  $\alpha$  indicates the angle of strain measurement with respect to the crack tangent (Fig. 7), and  $\varepsilon_{x'x'}$  is the strain measured by the gage. Use of the above equations precludes non-planar specimen geometries such as plates with side-grooves. In Eq. (10), in-plane stress intensity factors and singular term coefficients are related by

$$A_0 = \frac{K_I}{\sqrt{2\pi}} \quad (11)$$

$$C_0 = \frac{K_{II}}{\sqrt{2\pi}} \quad (12)$$

Using Eqs. (10)–(12), stress intensity factors can be obtained from strain gages by any sufficient combination of the following:

- (1) Eliminating terms by assumption. For example, assumption of a purely mode I field eliminates the terms with coefficients  $C_0$ ,  $C_1$ , and  $D_1$ . In addition, the contribution of higher order terms may be negligible in comparison to the leading terms.
- (2) Eliminating terms by gage orientation. Gage placement and orientation angles can be chosen to eliminate up to two terms.
- (3) Using additional gages. With one gage per unknown coefficient, each positioned to provide unique information, the coefficients can be determined using linear algebra. By using additional gages the system of equations is overdetermined and the coefficients can be obtained by a least-squares fit.

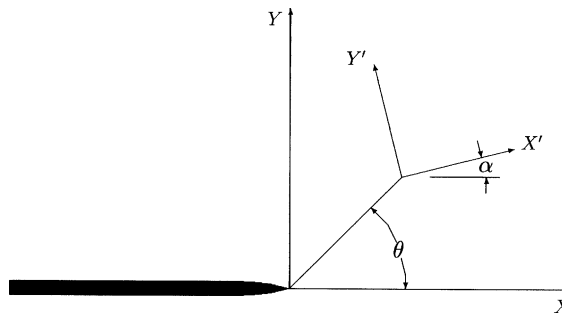


Fig. 7. Coordinate system for strain gage placement and orientation.



The combination of tactics employed must be guided by the fact that only so many gages can be physically located around the crack tip—each gage must be located beyond crack tip plastic deformation but within the area described by the asymptotic terms used. Stress intensities and speeds of propagating cracks may be measured by locating strain gages ahead of the initial crack tip oriented with respect to anticipated crack tip location. While Eq. (7) is for a stationary quasistatic crack, the singular terms are the same for any crack condition so long as crack speed is much less than the material shear wave speed. Generalizations of the above approach to dynamic crack growth are also possible.

3.4.2. Implementation

The methodology for measuring  $K_I^d$  is adopted from the work of Dally and Burger [19]. For mode I cracks ( $C_0 = C_1 = D_1 = 0$ ) the coefficient of  $B_0$  is 0 if the strain gage orientation angle  $\alpha$  is chosen such that

$$\cos 2\alpha = -k = -\frac{1 - \nu}{1 + \nu} \tag{13}$$

and the coefficient of the  $A_1$  term is likewise eliminated by choosing strain gage position angle  $\theta$  so

$$\tan \frac{\theta}{2} = -\cot 2\alpha \tag{14}$$

For a single strain gages positioned in this manner, its output will be related to  $K_I^d$  by

$$2\mu\epsilon_{x'x'} = \frac{K_I^d}{\sqrt{2\pi r}} \left[ k \cos \frac{\theta}{2} - \frac{1}{2} \sin \theta \left( \sin \frac{3\theta}{2} \cos 2\alpha - \cos \frac{3\theta}{2} \sin 2\alpha \right) \right] + O(r) \tag{15}$$

Both angles are functions of Poisson’s ratio  $\nu$  and are tabulated in Table 1. The relative contribution of higher order terms can be detected by comparing values from two gages placed at different radii.

For the simplest case of  $\nu = 1/3$ ,  $\alpha = \theta = 60^\circ$  and

$$K_I^d = E \sqrt{\frac{8}{3}} \pi r \epsilon_g \tag{16}$$

where  $\epsilon_g = \epsilon_{x'x'}$  is the strain gage output.

Usually the strain measured by a gage is taken to be the value at an infinitesimal point located at the center of the gage. Since the actual strain field measured does not vary linearly with  $r$ , this approximation introduces error for a gage of finite area. By assuming a  $K_I$ -field with strain measured by a strain gage positioned as described above, Dally and Burger [19] show that the radius  $r$  used in conjunction with the strain gage measurement should not be that to the center of the gage ( $r_0$ ), but instead  $r_0 - \Delta r$ , with  $\Delta r$  given by

$$\frac{\Delta r}{r_0} = \frac{1}{2} \left\{ 1 - \left[ 1 - \left( \frac{L}{2r_0} \right)^2 \right]^{1/2} \right\} \tag{17}$$

where  $L$  is the strain gage’s gage length. In practice, minimal gage location radius is limited to the maximum of half strain gage size (for which gradient-error must be corrected), three-dimensional zone radius (equal

Table 1  
Strain gage angles to measure  $K_I^d$  with single strain gage

| $\nu$ | $\theta$ (deg) | $\alpha$ (deg) |
|-------|----------------|----------------|
| 0.250 | 73.74          | 63.43          |
| 0.300 | 65.16          | 61.29          |
| 0.333 | 60.00          | 60.00          |
| 0.400 | 50.76          | 57.69          |
| 0.500 | 38.97          | 54.74          |

to half the specimen thickness) where plane stress assumptions for Eq. (10) begin to fail, and extent of any anticipated shear lips, which is more of a problem with running cracks. The gage also must be located within the region of dominance associated with the asymptotic terms used, the closer to the crack tip the better as the desired singular term will be more dominant. Often the gradient-error correction will be less than the uncertainty in strain gage position. The gradient-error correction depends on gage position and orientation, as well as on the stress terms anticipated to be present—Eq. (17) is for a gage placed with  $\alpha = \theta = 60^\circ$  in a pure  $K_I$ -field only. The constraints on gage location, however, is the same for all configurations.

### 3.5. Coherent gradient sensing

CGS is a full-field optical interferometric method which can measure surface slopes for reflective specimens and geometric and stress induced optical path gradients for transparent specimens [20,21,24]. CGS produces fringes which can be related to gradients of  $\hat{\sigma}_{11} + \hat{\sigma}_{22}$  for flat plates deforming under plane stress conditions. This information can then be compared to predictions by fracture models to extract fracture/field parameters. Usually fringe patterns of crack tip singularities are analyzed within the context of LEFM. CGS has similarities to the optical method of caustics [22–24] but provides full-field measurement. Its sensitivity to *gradients of displacements* makes it ideal for measuring singular fields such as those about a crack tip. Other optical techniques which instead measure *displacements*, such as moiré interferometry [25], can provide useful fringe patterns only within a small displacement range and thus have limited utility in singular fields. CGS is insensitive to rigid body motions and vibrations and is well suited for high speed photography, making it an ideal measurement technique for dynamic fracture studies. While in principle CGS is applicable to quasistatic fracture measurement, in practice crack tip mechanical fields of reasonably sized ASTM standard C(T) and bend specimens are influenced by load point fields and boundary effects. While such effects have minimal influence very close to the crack tip, they are significant in much of the area interrogated by CGS, rendering fringe patterns difficult to analyze.

In practice the implementation of CGS requires extensive specimen preparation. For opaque materials, one surface must be made optically flat and highly reflective. In metals this may be accomplished by lapping, polishing, and, if necessary, depositing a thin layer of highly reflective aluminum. The experimental setup is complex. Fringe pattern images must be captured by high speed photography which requires precise timing, accurate triggering, and careful optical alignment.

#### 3.5.1. Governing equations

A full description of the CGS technique can be found in Ref. [24]. CGS can be employed in either a reflection (Fig. 8) or transmission (Fig. 9) configuration. In the reflection configuration a mirror-finished region of interest (optically flat prior to loading) is interrogated by an expanded collimated coherent laser beam. After the laser beam reflects off the deformed specimen surface, it passes through two diffraction gratings which process the beam to yield fringes of constant gradient of out-of-plane displacement. The fringe patterns from the first order diffraction are imaged using a focusing lens, an aperture, and a high speed camera.

In transmission mode the interrogating laser beam passes through a transparent specimen and is influenced by geometric and stress induced optical property changes before being processed by the two diffraction gratings. Assuming plane stress conditions, the governing equation for reflection CGS is:

$$\frac{\partial u_3}{\partial \hat{x}} = -\frac{vh}{2E} \frac{\partial(\hat{\sigma}_{11} + \hat{\sigma}_{22})}{\partial \hat{x}} = \left(\frac{mp}{2A}\right), \quad m = 0, \pm 1, \pm 2, \dots \quad (18)$$

where  $u_3$  is the out of plane displacement,  $\hat{x}$  is the shearing direction or direction on the specimen plane perpendicular to the gratings' lines along which surface gradients are evaluated,  $h$  is the specimen out-of-

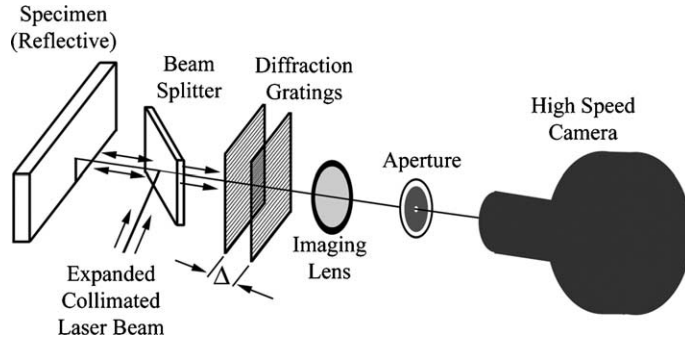


Fig. 8. Schematic of experiment setup for reflection CGS.

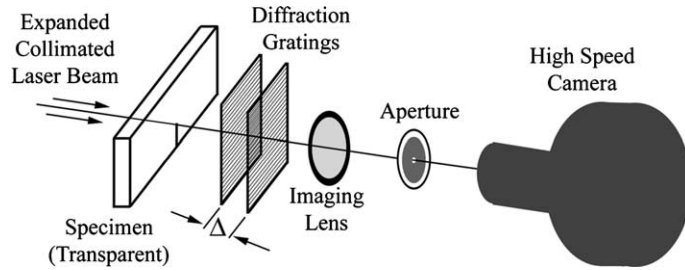


Fig. 9. Schematic of experiment setup for transmission CGS.

plane thickness,  $m$  is the fringe number (integer for constructive (light) fringes),  $p$  is the grating pitch, and  $\Delta$  is the distance between the pair of gratings.

The general transient elastodynamic crack tip asymptotic solution in terms of stress is then used (see extensive discussion by Freund and Rosakis [8]) with Eq. (18) to relate the CGS interferograms and the unknown asymptotic coefficients including the stress intensity factors:

$$\begin{aligned}
 \frac{mp}{\Delta ch} = & -K_I^d \frac{F_I(v)}{2\sqrt{2\pi r_1}^{3/2}} \left[ \cos \phi \cos \frac{3\theta_1}{2} + \alpha_1 \sin \phi \sin \frac{3\theta_1}{2} \right] \\
 & + \frac{1}{2\sqrt{r_1}} \left\{ \text{Re}[\eta_1] \left[ \cos \phi \cos \frac{\theta_1}{2} + \alpha_1 \sin \phi \sin \frac{\theta_1}{2} \right] \right. \\
 & + \text{Re}[\eta_2] \left[ \cos \phi \left( 2 \cos \frac{\theta_1}{2} - \cos \frac{5\theta_1}{2} \right) - \alpha_1 \sin \phi \left( 2 \sin \frac{\theta_1}{2} + \sin \frac{5\theta_1}{2} \right) \right] \\
 & \left. + \text{Re}[\eta_3] \left[ \cos \phi \left( 4 \cos \frac{5\theta_1}{2} - 3 \cos \frac{9\theta_1}{2} \right) - \alpha_1 \sin \phi \left( 4 \sin \frac{5\theta_1}{2} + 3 \sin \frac{9\theta_1}{2} \right) \right] \right\} \\
 & + K_{II}^d \frac{F_{II}(v)}{2\sqrt{2\pi r_1}^{3/2}} \left[ \cos \phi \sin \frac{3\theta_1}{2} - \alpha_1 \sin \phi \cos \frac{3\theta_1}{2} \right] \\
 & + \frac{1}{2\sqrt{r_1}} \left\{ \text{Im}[\eta_4] \left[ -\cos \phi \sin \frac{\theta_1}{2} + \alpha_1 \sin \phi \cos \frac{\theta_1}{2} \right] \right. \\
 & + \text{Im}[\eta_2] \left[ \cos \phi \left( 2 \sin \frac{\theta_1}{2} - \sin \frac{5\theta_1}{2} \right) + \alpha_1 \sin \phi \left( 2 \cos \frac{\theta_1}{2} + \cos \frac{5\theta_1}{2} \right) \right] \\
 & \left. + \text{Im}[\eta_3] \left[ \cos \phi \left( 4 \sin \frac{5\theta_1}{2} - 3 \sin \frac{9\theta_1}{2} \right) + \alpha_1 \sin \phi \left( 4 \cos \frac{5\theta_1}{2} + 3 \cos \frac{9\theta_1}{2} \right) \right] \right\}
 \end{aligned} \tag{19}$$

where

$$c = -\frac{v}{E} \quad (20)$$

$$F_1(v) = \frac{2(1 + \alpha_s^2)(\alpha_1^2 - \alpha_s^2)}{D(v)} \quad (21)$$

$$D(v) = 4\alpha_1\alpha_s - (1 + \alpha_s^2)^2 \quad (22)$$

$$\alpha_{1,s}(t) = \left(1 - \frac{v^2(t)}{c_{1,s}^2}\right)^{1/2} \quad (23)$$

$$r_1 = \left(x_1^2 + (\alpha_1 x_2)^2\right)^{1/2} \quad (24)$$

$$\theta_1 = \tan^{-1}\left(\frac{\alpha_1 x_2}{x_1}\right) \quad (25)$$

and  $v$  is the crack tip speed,  $c_1$  and  $c_v$  are the material longitudinal and shear wave speed respectively,  $\phi$  is the angle between the CGS shearing direction  $\hat{x}$  and the crack tip tangent, and the various  $\eta$  quantities are the unknown coefficients of the higher order asymptotic solution terms.

Since Eq. (19) is linear in the unknown coefficients, it is relatively straightforward to obtain a data set  $m(r_1, \theta_1)$  from each CGS interferogram to find the unknown coefficients including  $K_I^d$  and  $K_{II}^d$  using least-squares fitting. After the fit is performed a measure of fitting error can be computed by calculating the rms error between the value of the fringe number  $m$  from the digitization and subsequent fit as follows:

$$E = \frac{1}{N} \left( \sum_{n=1}^N \left( m_n(\underline{x}_n) - \hat{m}_n(\underline{x}_n) \right)^2 \right)^{1/2} \quad (26)$$

where  $m_n$  is the fringe number for the  $n$ th point as specified during digitizing,  $\hat{m}_n$  is the fringe number calculated from the fit at the same location using Eq. (19), and  $N$  is the total number of data points. Given an error metric, the location of the crack tip can be assumed to be in the location which results in a minimal fitting error. While the crack tip location chosen by this approach may not coincide with the actual crack tip due to blunting, tunneling, etc. its objectivity makes it ideal for determining crack initiation and crack tip velocities. Furthermore, by minimizing an error it is ensured that the crack tip stress fields are optimally fit to analytic asymptotic fields. The least troublesome method of locating the crack tip is by systematically “searching” over a gridded region known to contain the crack tip.

### 3.5.2. Implementation

Prior to testing, the specimen faces were lapped to make them optically flat, then polished to allow the interrogating laser beam to reflect off the surface. After fatigue pre-cracking, the specimens were ready for testing. For this work the same high speed camera and illuminating laser were used as for the COD technique. Kodak TMAX-400 black and white film was used to record the interferograms at regular time intervals during dynamic loading, crack initiation, and propagation. Following the tests, the photographic negatives were developed and scanned. Using a custom made Matlab code and graphical user interface created for this work, the CGS fringes were overlaid with radial lines at regular lines from the crack tip. Data taking was done by hand by indicating the location and fringe number where the fringes intercept the radial lines. This data was then fit using Eq. (19) after filtering out data inside the three-dimensional zone to

determine the unknown coefficients and stress intensity factors. The Matlab code includes provisions for utilizing mode I pre-initiation data from inside the three-dimensional zone, but since the interferograms contained sufficient data away from the crack tip, this feature was unnecessary and not used.

### 3.5.3. Comments

As a full-field measurement technique, CGS supplies the most detailed crack information regarding the near-tip mechanical field of the three dynamic stress intensity factor measurement techniques. With sufficiently sophisticated data analysis, this technique can be used to provide stress intensity factor measurements for any combination of mode I and mode II loading, as well as the coefficients of the higher order terms of the crack tip asymptotic solution used. Given higher order term coefficients, the size of the  $K$  dominated field can be examined to determine  $K$ -dominance assumption validity. Crack tip position can also be determined from CGS interferograms and used to establish initiation time and calculate crack speed. By analyzing many well timed images from a single test, CGS can measure loading rate, mixed mode initiation toughness, propagation toughness, and crack speed.

No CGS tests were conducted on side-grooved specimens as no simple relationship exists between CGS fringe patterns and the crack tip stress field for this geometry. Another shortcoming with CGS is that the specimen material/geometry must maintain reflectivity and produce analyzable fringe patterns during the loading and failure process.

## 4. Experimental comparison of techniques

### 4.1. Experimental setup

The material used for all comparisons is a commercially pure 6Al–4V titanium alloy with nominal properties given in Table 2.

All specimens were cut from titanium plate having a nominal thickness of 12.7 mm. All specimens use three point bend geometry with overall in-plane dimensions of 100 mm × 250 mm. The lower span in all dynamic tests is 230 mm. While some may debate whether initiation toughness depends on instantaneous loading rate  $\dot{K}$  at initiation or on some average loading rate over time, use of this tall bend specimen geometry tends to produce dynamic loading rates that are fairly constant rendering this finer point immaterial. The instantaneous loading rate at initiation is reasonably close to the average loading rate. The large in-plane dimensions are also necessary to allow crack tip mechanical fields to develop free of boundary effects, even after initiation and some propagation, which is of particular importance for the CGS technique.

Sharp pre-cracks were produced by first cutting a 31.8 mm notch using wire EDM and then fatiguing 2 mm of crack extension. Side-grooves were cut by plunge EDM in some specimens according to ASTM

Table 2  
Nominal properties of commercial grade 6Al–4V titanium alloy

|                    |   |
|--------------------|---|
| Ultimate stress    | 860 MPa (125 ksi)                                 |
| Yield stress       | 790 MPa (115 ksi)                                 |
| Young's modulus    | 120 GPa (17 400 ksi)                              |
| Poisson's ratio    | 0.32  |
| Tensile elongation | 10%   |
| Reduction of area  | 25%   |
| Hardness           | $R_c = 35$  |
| Density            | 4.5 g/cm <sup>3</sup> (0.16 lb/in. <sup>3</sup> ) |

standard E647-00. Side-groove depth is indicated by total thickness reduction by the grooves as a percentage of the specimen's ungrooved thickness. Side-grooves specimens can be thought of as behaving like a thinner specimen with reinforcement material adjacent to the crack or as a thicker specimen with shear lips "pre-machined" off. Ultimately the side-grooves' effect is to cause the crack to exist in more of a plane strain condition and thus allow the measurement of plane strain fracture toughness.

In tests performed on ungrooved specimens of the 6Al-4V Ti, shear lips grew to nearly 33% of the specimen thickness in dynamic tests after 10–15 mm of crack growth (versus 100% for quasistatically tested specimens of the same thickness). These shear lips would render the strain gage technique unable to measure toughness of propagating cracks, but since the shear lip development is delayed, strain gages could be used to measure crack initiation toughness.

Data is given from tests using 3 and 9 m/s impact speeds. In all plots, initiation time is indicated by a vertical dashed line. Strain gage and CGS data are obtained simultaneously from the same experiments. COD data from specimens with and without side-grooves are shifted temporally to share initiation time with the strain gage/CGS test of the same impact speed.

For comparison, a side-grooved CT specimen was tested quasistatically, giving a toughness  $K_{Ic}$  of 91.3 MPa $\sqrt{m}$ . The quasistatic characteristic plastic zone size (Eq. (2)) is 2.5 mm. The plastic zone size is smaller under dynamic effects due to loading rate effects on yield stress.

#### 4.2. 3 m/s impact speed test results

Stress intensity histories are given in Fig. 10 from three tests using 3 m/s impact speeds. The first test utilized a strain gage and CGS to simultaneously measure the stress intensity factor as a function of time. Overall agreement is good though the initiation value  $K_{Ic}^d$  from the strain gage is 13% less than that from CGS. Two COD tests were run, one on a specimen with side-grooves and the other without. Both COD tests match the CGS data well. The specimen with 22.1% side-grooves initiate more quickly after impact than the two specimens without side-grooves—this is manifest in the plot as a delay of about 60  $\mu$ s before loading starts as compared to the other tests because the three tests are plotted such that the crack initiation times coincide. Crack initiation time for the strain gage trace is taken to be the time at peak strain. CGS fringes also provides crack tip location (Fig. 11) through the fit error minimization which indicates an initiation time which agrees well with the strain gage initiation time. The noise in crack tip location prior to

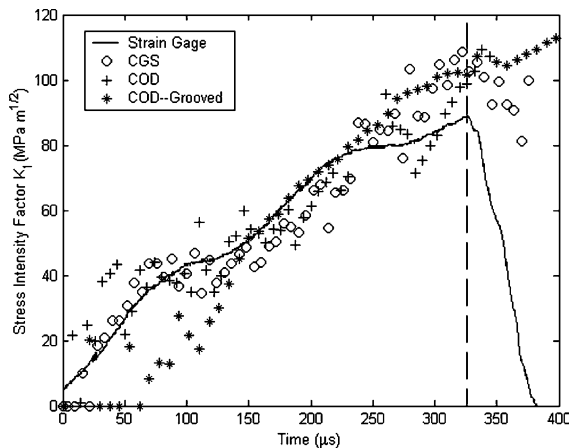


Fig. 10. Comparison of dynamic stress intensity factors  $K_{I1}^d$  versus time as obtained by different measurement methods for 6Al-4V Ti specimens impacted at 3 m/s.

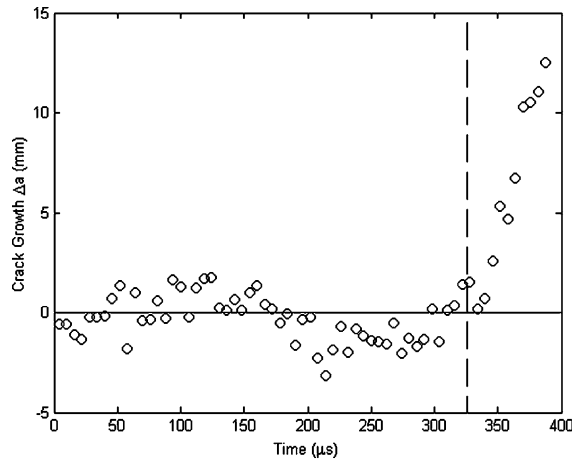


Fig. 11. Crack tip position versus time as obtained by CGS for a 6Al-4V Ti specimen impacted at 3 m/s.

initiation is typical and is due primarily to imprecision of locating a fixed reference point on the specimen and the limited amount of fringe data during early loading stages. CGS crack tip location data was invaluable for establishing the validity of COD crack initiation detection methodology.

Fig. 12 shows crack opening angle versus time from the ungrooved specimen. From 150 to 325  $\mu\text{s}$  the opening angle remains fairly constant, after which the angle increases rapidly. The jump in opening angle is taken to indicate that crack initiation has occurred. Up through this initiation time the calculated stress intensity factor from COD measurement is in good agreement with the strain gage and CGS results. For the side-grooved specimen no distinct change in COD opening angle appears, however the values of  $K_I^d$  appear to drop slightly at initiation and then to jump (Fig. 10). This occurs at values consistent with the other two tests. In the absence of the other results it is doubtful that initiation time and thus  $K_{Ic}^d$  could be determined with much confidence. The determination of crack initiation time is a common obstacle in initiation toughness measurement.

Fig. 13 shows a sequence of CGS images at 18, 163, 326, and 388  $\mu\text{s}$ . These times are at the beginning of loading, midway to initiation, initiation, and post-initiation respectively. The crack extends upward from the bottom of each image. The position of the zeroth order fringe is indicated by a “0.” The first image shows that the specimen surface has slight curvature prior to loading which is manifest as a wide horizontal dark fringe above the crack tip. The second image looks very much like the theoretical fringe patterns from a  $K_I$ -field except, unfortunately, the fringe intensities are reversed due to some combination of the initial curvature and wave loading. Here fringe numbering was chosen as indicated to reconcile best with previous and subsequent images in the test sequence. Temporally local fringe numbering difficulties like this are not unusual. By initiation the fringes look typical, and after initiation the fringe patterns are highly distorted but the rear lobes are still analyzable. Typically, the front lobe (ahead of the crack tip) is the most prone to be distortion by loading waves and by structural specimen flexing as exemplified in the third and fourth fringe patterns. The best data usually comes from the rear lobes. These fringes are all analyzable using higher order terms and other features employed in the Matlab analysis suite.

Fig. 14 shows COD profiles for a crack at about the same times as the CGS images above, except for the fourth profile which is 44  $\mu\text{s}$  earlier. The length of the EDM notch initially visible is 12.71 mm, and the crack tip, which cannot be seen, is located about 2 mm above the top of the EDM notch. It is obvious that the notch widens as the crack loads, but little else can be observed without digitizing the profile and post-processing.

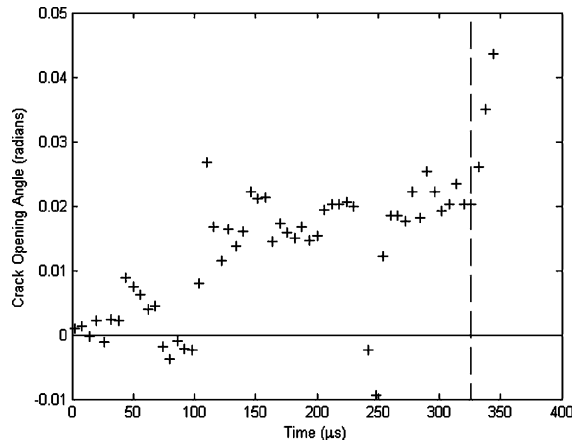


Fig. 12. Crack/EDM notch opening angle versus time for a 6Al-4V Ti specimen with no side-grooves impacted at 3 m/s.

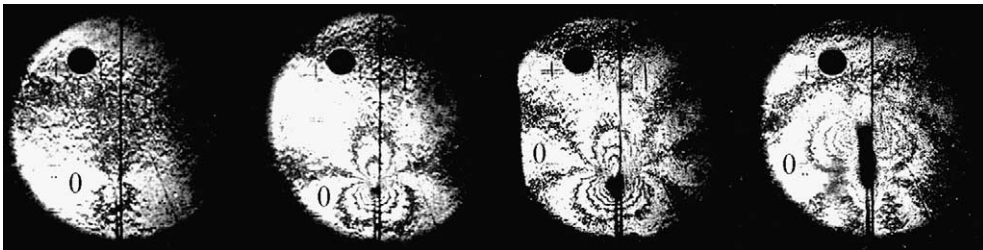


Fig. 13. CGS fringe patterns at (left to right) 18, 163, 326, and 388  $\mu$ s for a 6Al-4V Ti specimen impacted at 3 m/s (beam diameter = 50 mm).



Fig. 14. COD profiles at (left to right) 20, 164, 326, and 344  $\mu$ s for a 6Al-4V Ti specimen (no side-grooves) impacted at 3 m/s (initial notch length visible = 12.71 mm). Note that digital image processing is required to extract meaningful data.

Four COD profiles for the side-grooved specimen are shown in Fig. 15, each at the same times as the four CGS fringe patterns. The length of the EDM notch initially visible is 10.57 mm. Again it is apparent that the notch opens measurably from image to image, but further information is not obtainable without digitizing and post-processing.



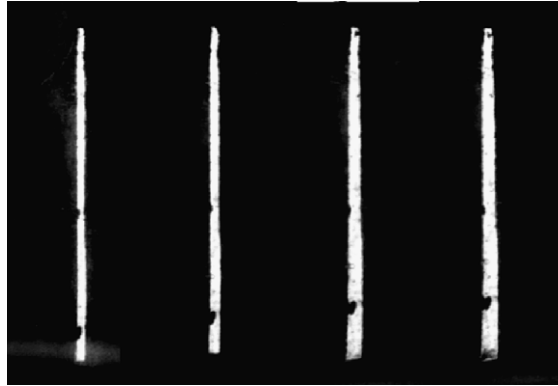


Fig. 15. COD profiles at (left to right) 22, 166, 326, and 390  $\mu\text{s}$  for a *side-grooved* 6Al-4V Ti specimen impacted at 3 m/s (initial notch length visible = 10.57 mm).

#### 4.3. 9 m/s impact speed test results

Three similar tests were also conducted using a 9 m/s drop weight impact speed. For the first test, the initiation value  $K_{Ic}^d$  from the strain gage is 18% higher than the same from CGS. Both COD tests match the CGS data fairly well also. If the COD data for the specimen without side-grooves were offset in time to superimpose the loading portion with the strain gage data, the agreement in initiation toughness would be excellent (Fig. 16). This suggests that the identification of initiation time is key to determining the value of  $K_{Ic}^d$  from COD measurements. Again the side-grooved specimen (23%) initiates more quickly after impact than those specimens without side-grooves. As before, initiation time for the strain gage trace is taken to be the time at peak strain. The CGS measured crack tip location history indicates the same initiation time (Fig. 17). For the COD measurements on the ungrooved and grooved specimens, crack initiation was indicated by a jump in crack opening angular velocity (Fig. 6).

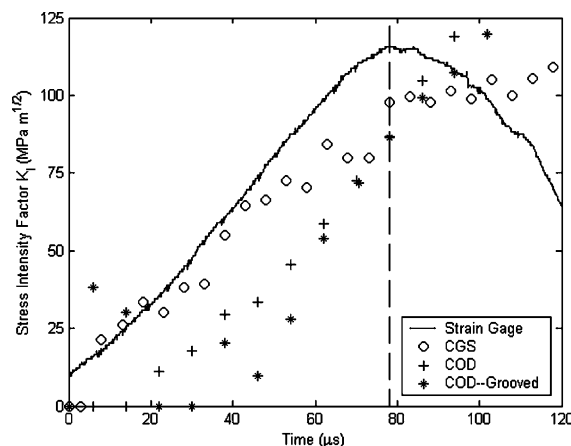


Fig. 16. Comparison of dynamic stress intensity factors  $K_{Ic}^d$  versus time as obtained by different measurement methods for 6Al-4V Ti specimens impacted at 9 m/s.

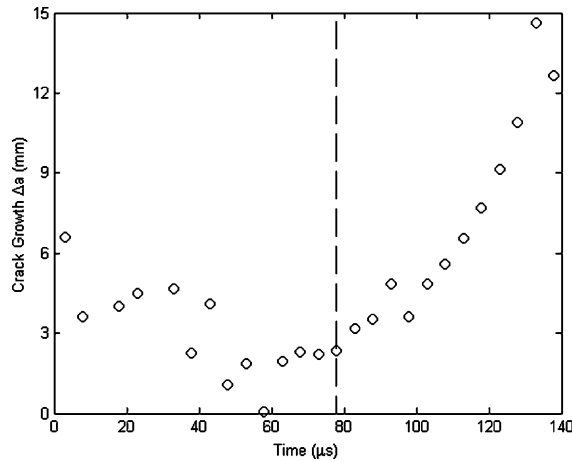


Fig. 17. Crack tip position versus time as obtained by CGS for a 6Al-4V Ti specimen impacted at 9 m/s.



Fig. 18. CGS fringe patterns at (left to right) 3, 38, 78, and 138  $\mu$ s for a 6Al-4V Ti specimen impacted at 9 m/s (beam diameter = 50 mm).

Fig. 18 shows a sequence of CGS images at 3, 38, 78, and 138  $\mu$ s which are at the beginning of loading, midway to initiation, initiation, and post-initiation respectively. The crack extends upward from the bottom of each image. The position of the zeroth fringe number is indicated by a "0." As with the 3 m/s test, the first image shows that the specimen surface has slight curvature prior to loading. The remaining fringe patterns are affected by this curvature, but are otherwise straightforward to analyze. Fig. 19 shows COD profiles for a crack at about the same times as above. The EDM notch initially visible is 10.82 mm long and the crack tip, which cannot be seen, is located about 2 mm above the EDM notch. The same for side-grooved specimen are shown in Fig. 20, all at the same times as the CGS fringe patterns. For this specimen the amount of EDM notch initially visible is 10.95 mm. Again it is apparent that the notch opens measurably from image to image, but further information is not obtainable without digitizing and post-processing. The fatigue crack is visible in the final image, but no light passes through behind the propagating crack.

The agreement between COD measurements from specimens with and without side-grooves suggests that in this dynamic loading regime the ungrooved specimens are thick enough to produce plane strain fracture toughness values.



Fig. 19. COD profiles at (left to right) 6, 38, 78, and 142  $\mu$ s for a 6Al–4V Ti specimen (no side-grooves) impacted at 9 m/s (initial notch length visible = 10.82 mm).

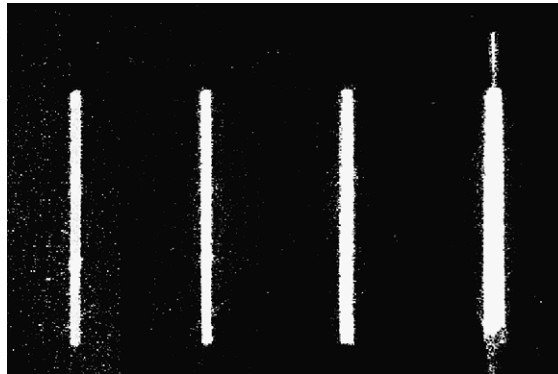


Fig. 20. COD profiles at (left to right) 6, 38, 78, and 142  $\mu$ s for a *side-grooved* 6Al–4V Ti specimen impacted at 9 m/s (initial notch length visible = 10.95 mm).

## 5. Conclusions

As implemented, the three experimental techniques for measuring dynamic crack tip stress intensity factor time histories, i.e., strain gage measurement, COD, and CGS provide very similar values for the 6Al–4V Ti tested. Variation in results may be due to measurement error and natural variation in real materials. Therefore, obtaining dynamic initiation toughness values for an engineering material using three fundamentally different techniques which agree to this level must be considered a success. Some comments on each technique's strengths and weaknesses, as well as commentary on measurement error follow. In general, measurement error for each technique has significant dependence on the materials and geometries tested.

CGS as employed is the most robust technique of the three. Because it is a full-field technique the fracture parameters obtained can be verified against the CGS measurements. The obtainment of higher order terms of the crack tip asymptotic solution allows verification of  $K$ -dominance. Finally a fitting error can be used not only to quantify how well the LEFM asymptotic solution correlates with the measured crack tip mechanical fields, but to objectively track crack tip position to obtain initiation time and crack tip velocity. Measurement error can be estimated to some degree from the noise in  $K$  versus time plots. For this work an error estimate of 10% is a conservative upper bound. Systematic error is negligible as the analysis assumptions are upheld by the fact that the fit is dominated by the  $K$ -field. In general a feel for

measurement error can be gained from the various analysis results. Typically this technique is expected to be the most accurate, otherwise the analysis will indicate that something is amiss. The chief drawback is that this technique requires a complicated and expensive experimental setup and significant specimen preparation.

The strain gage technique proves itself as an easy, inexpensive method to obtain stress intensity factors. The assumption that the measured strain is maximum at initiation is supported by CGS results. The fact that results from a single gage measuring strain in the neighborhood of one point agrees well with CGS results is encouraging. Measurement error for the strain gage technique is about 15% as judged against the CGS results. In the absence of data from alternative measurement techniques, strain gage technique error can generally be estimated by redundancy of measurement. The considerable advantage of this technique is very simple and inexpensive compared to the other techniques.

Finally, the COD technique proved itself useful for specimens without and with side-grooves. It is the only technique of the three that works with side-grooved specimens, otherwise the other techniques are preferable in terms of their respective advantages. The two comparisons of measurement results suggests that the enabling assumptions made for employing COD technique in this work are reasonable and justified. A pressing need for COD technique is a more accurate method of determining initiation time. For this work the opening angle between the faces of the EDM notch suffices, but only because of verification afforded by the other measurement techniques. While strain gages can be used to detect initiation in un-grooved specimens, specimens with side-grooves may require the use of some alternative method. Measurement error for specimens with and without side-grooves was about 13% at one impact speed and only a couple percent in the other. Generally the error can be directly attributed to the resolution at which the crack opening can be ascertained and error associated with the accuracy of crack initiation time determination. This technique in general may be hit or miss depending on whether measurements and analysis assumptions are of sufficient quality.

## Acknowledgements

The authors would like to acknowledge the gracious support of the Office of Naval Research (Steels) program and Dr. Julie Christodoulou, program officer, under contract number N00014-01-1-0937. We would also like to extend our gratitude to Prof. G. Ravichandran (Caltech) for his insights shared over numerous conversations.

## References

- [1] Irwin GR. Analysis of stresses and strains near the end of a crack traversing a plate. *J Appl Mech* 1959;24:361–4.
- [2] Williams ML. On the stress distribution at the base of a stationary crack. *J Appl Mech* 1957;24:109–14.
- [3] American Society for Testing and Materials, West Conshohocken, PA 19428-2959, Annual Book of ASTM Standards 2001 Sect. 3 Metals Test Methods and Analytic Procedures; Volume 03.01, Metals—Mechanical Testing; Elevated and Low Temperature Tests; Metallography.
- [4] Ravi-Chandar K, Knauss WG. An experimental investigation into dynamic fracture: I. Crack initiation and arrest. *Int J Fract* 1984;25:247–62.
- [5] Maigre H, Rittel D. Dynamic fracture detection using the force-displacement reciprocity: application to the compact compression specimen. *Int J Fract* 1995;73:67–79.
- [6] Rittel D, Maigre H. A study of mixed-mode dynamic crack initiation in PMMA. *Mech Res Commun* 1996;23:475–81.
- [7] Rittel D, Maigre H. An investigation of dynamic crack initiation in PMMA. *Mech Mater* 1996;23:229–39.
- [8] Freund LB, Rosakis AJ. The structure of the near tip-field solution during transient elastodynamic crack growth. *J Mech Phys Solids* 1992;40:699–719.

- [9] Suresh S, Nakamura T, Yeshurun Y, Yang KH, Duffy J. Tensile fracture-toughness of ceramic material—effects of dynamic loading and elevated-temperatures. *J Am Ceram Soc* 1990;73:2457–66.
- [10] Wilson ML, Hawley RH, Duffy J. The effect of loading rate and temperature on fracture initiation in 1020 hot-rolled steel. *Engng Fract Mech* 1980;13:371–85.
- [11] Dally JW. Dynamic photoelastic studies of fracture. *Exp Mech* 1979;19:349–67.
- [12] Rosakis AJ, Duffy J, Freund LB. The determination of the dynamic fracture toughness of AISI 4340 steel by the shadow spot method. *J Mech Phys Solids* 1984;34:443–60.
- [13] Zehnder AT, Rosakis AJ. Dynamic fracture initiation and propagation in 4340 steel under impact loading. *Int J Fract* 1990;43:271–85.
- [14] Owen DM, Zhuang S, Rosakis AJ, Ravichandran G. Experimental determination of dynamic crack initiation and propagation fracture toughness in thin film aluminum sheets. *Int J Fract* 1998;90:153–74.
- [15] Shih CF. Relationships between the  $J$ -integral and the crack opening displacement for stationary and extending cracks. *J Mech Phys Solids* 1981;29(4):305–26.
- [16] Hutchinson JW. Singular behavior at the end of a tensile crack in a hardening material. *J Mech Phys Solids* 1968;16:13–31.
- [17] Rice JR, Rosengren GF. Plane strain deformation near a crack tip in a power law hardening material. *J Mech Phys Solids* 1968;16:1–12.
- [18] Dally JW, Burger JR. The role of the electric resistance strain gage in fracture research. In: Epstein JS, editor. *Experimental Techniques in Fracture*. VCH Publishers; 1993. p. 1–39 [chapter 1].
- [19] Tippur HV, Krishnaswamy S, Rosakis AJ. A coherent gradient sensor for crack tip deformation measurements: analysis and experimental results. *Int J Fract* 1990;48(1):193–204.
- [20] Tippur HV, Krishnaswamy S, Rosakis AJ. Optical mapping of crack tip deformations using the methods of transmission and reflection coherent gradient sensing: a study of crack tip  $K$ -dominance. *Int J Fract* 1991;52:91–117.
- [21] Theocaris PS. Elastic stress intensity factors evaluated by caustics. In: Shih GC, editor. *Mechanics of Fracture*, vol. VII. The Netherlands: Sijthoff and Noordhoff, Roc Alphen aan den Rijn; 1981.
- [22] Kalthoff JF. Shadow optical methods of caustics. In: Kobayashi AS, editor. *Handbook on Experimental Mechanics*. New York, NY: McGraw-Hill; 1987. p. 430–98 [chapter 9].
- [23] Rosakis AJ. Two optical techniques sensitive to gradients of optical path difference: the method of caustics and the coherent gradient sensor (CGS). In: Epstein JS, editor. *Experimental Techniques in Fracture*. VCH Publishers; 1993. p. 327–425 [chapter 10].
- [24] Post D. High sensitivity moire experimental analysis for mechanics and materials. 2nd ed. Boca Raton, FL 33431: CRC Press; 1995.
- [25] Williams ML. Bearing pressures and cracks. *J Appl Mech* 1939;6:49–53.
- [26] Westergaard HM. On the stress distribution at the base of a stationary crack. *J Appl Mech* 1959;24:109–14.
- [27] Sneddon IN. The distribution of stress in the neighbourhood of a crack in an elastic solid. *Proc Roy Soc Lond A* 1946;147:229–60.
- [28] Freund LB. *Dynamic fracture mechanics*. New York, NY: Cambridge University Press; 1998.